Hybrid Control of a Turret Wake

Bojan Vukasinovic* and Ari Glezer†
Georgia Institute of Technology, Atlanta, Georgia 30332-0405
Stanislav Gordeyev‡ and Eric Jumper§
University of Notre Dame, Notre Dame, Indiana 46556
and
Valdis Kibens¶
The Boeing Company, Saint Louis, Missouri 63166

Effects of hybrid flow control and its active and passive components on the aerodynamic characteristics of flow over a 0.254-m-diam conformal optical aperture embedded in the hemispherical cap of a cylinder turret model ($D = 0.61$ m) are investigated at $M = 0.3$–0.5 and $Re_D = 4.4$–7.4×10^6. Resulting mean flows are characterized by surface static pressure distributions and oil-flow visualizations, while the separated-flow dynamics are assessed by hot-film measurements. Active flow control is effected by arrays of piezoelectrically driven synthetic jet modules distributed in multiple arrays upstream from the aperture. Active flow control is further assisted by global flow alterations induced by a passive forward partition plate, and, when combined, constitute hybrid flow control. It is shown that the hybrid flow control combines the positive effects of its component control elements to yield superior results in any cumulative aerodynamic aspect of the separated flow. This cumulative effect of the actuation is manifested by concomitant delay of flow separation and active, dissipative suppression of turbulent motions downstream of separation. It is also demonstrated by means of direct two-dimensional wave-front measurements that the overall aerodynamic improvements correlate with substantial suppression of optical aberrations through the separated flow. Furthermore, estimated Strehl ratios for the laser beam indicate that nearly invariant Strehl ratio is established within the range of tested aperture elevation angles, yielding improvement of about 50% for the highest elevation angle.

Nomenclature

A_j	=	exit area of the actuator orifice
A_o	=	frontal turret area
C_p	=	pressure coefficient
C_μ	=	jet momentum coefficient
D	=	turret diameter
f_d	=	actuation frequency
H	=	height of turret base
M	=	Mach number
OPD_{rms}	=	root mean square of optical path difference
R	=	turret radius
Re_D	=	Reynolds number
St_D	=	Strouhal number
U_j	=	average jet velocity
U_0	=	freestream velocity
α	=	azimuthal angle of pressure ports
γ	=	elevation angle of optical window
γ_s	=	flow-separation angle
ρ	=	air density

*Research Engineer, Woodruff School of Mechanical Engineering. Member AIAA.
†Professor, Woodruff School of Mechanical Engineering. Associate Fellow AIAA.
‡Assistant Research Professor, Department of Aerospace and Mechanical Engineering. Member AIAA.
§Professor, Department of Aerospace and Mechanical Engineering. Fellow AIAA.
¶Technical Fellow, Phantom Works, Mail Code S306-430, P.O. Box 516. Associate Fellow AIAA.

I. Introduction

TURRETS on airborne platforms are bluff-body protrusions that typically consist of a spherical cap supported by a matching cylindrical base. They provide convenient housing for pointing and tracking laser beams from airborne platforms. An optical aperture is therefore built into the turret cap, and can be either flat or conformal. Turrets create wakes that can distort an otherwise planar laser beam [1], even at relatively low subsonic speeds. Consequently, this leads to the laser beam's unsteady defocus and jitter [2].

When an optical wave front passes through a variable index-of-refraction turbulent flow, its wave front becomes distorted or aberrated and these distortions are referred to as an aero-optical problem [2]. These wave-front distortions, combined with optical aberrations caused by the wave-front propagation through the atmosphere, known as an atmospheric propagation problem [3], ultimately degrade the light intensity from the otherwise diffraction-limited intensity at the destination. These aberrations have high spatial and temporal bandwidths which are well outside the current control capabilities of traditional adaptive-optics methods [4]. Separated shear layers, such as those in the wakes of bluff bodies, are particularly destructive because of the presence of large coherent vortical structures that are known to be a major source of optical wave-front distortion [5], since they induce strong pressure and density gradients [6]. Left untreated, these shear-layer-related optical aberrations can limit an airborne transmitting system to a forward-looking quadrant only. To extend viewing angles to at least a portion of an aft-looking quadrant, a region of the attached flow can be extended by delaying separation of the flow and/or by disrupting formation of the large-scale shear layer vortices. The intent of the work presented in this paper is to evaluate the effectiveness of combined active and passive suppression of the unsteady aerodynamic environment for achieving significant improvement in light transmission efficiency by minimizing laser wave-front degradation. Control of the flow over a bluff-body turret that houses a laser-based optical system must satisfy more demanding requirements than separation control over external aerodynamic surfaces. Whereas the effectiveness of flow control on aerodynamic surfaces can be evaluated in terms of its effect on the

time-averaged aerodynamic forces and moments, when the intent of flow control is to enhance transmission of optical wave fronts through regions of separated turbulent flow, spatial and temporal flow dynamics need to be evaluated, rather than just static (mean) effects on the flow.

A flow over a typical turret geometry can be considered as a part of the class of flows over a surface-mounted obstacle having a free end [7]. A common feature of the separated flows behind any of these surface-mounted obstacles is that the resulting separated-flow topology is dominated by three major sources of vorticity: at the juncture of the protuberance and its support surface, over its main body, and at the free end. Furthermore, if the turret's aperture is flat, an additional source of vorticity is introduced at the aperture circumference, unless it has already been fully traversed by the separated flow. The relative contribution of each of these sources depends on the aspect ratio of the obstacle as well as the specifics of the geometry cross-sectional profile. As the geometry under consideration can be considered a circular cylinder with a modified free end, it is to be expected that the separated flow is dominated by vortices shed off the "free-end" tip (i.e., the hemispherical cap), off the cylinder body, and at the cylinder base. A relative contribution of these three sources clearly depends on the turret's height-to-radius ratio H/R. When the support height is commensurate with the turret radius, it is expected that the wake topology would depend on all the sources of vorticity. Having the cap elevated to multiple radii [8] increases the relative importance of the cylindrical support and the wake becomes dominated by vortices shed off the cylindrical support. Conversely, when the support cylinder height is less than the radius, it is expected that shedding of the cylinder body becomes less important. In the limit case, the cylindrical support vanishes completely, and the turret geometry becomes either a hemispherical or spherical shell [9,10]. In such a case, the relative importance between vortices shed off the surface and formed at the juncture depends on the ratio of the incoming boundary-layer thickness and the protrusion height. With an increase of this ratio, necklace vortices formed about the juncture between the protrusion and support surface become more prominent. It should be noted that in Earth flows, it is often observed that the whole protrusion is immersed into the surface boundary layer, but such cases are of less importance for airborne platforms.

Some previous work on flow control of separated flows over bluff-body protrusions has been directly motivated by the aero-optical problems involving an aircraft turret. Passive modifications of the turret geometry were tested by Snyder et al. [11], who considered additions of aft-mounted fairings and splitter plates. They showed reduction of the baseline drag up to 55% by using a large fairing. The separated flow behind the turret with a flat aperture and the effects of passive control on the optical aberrations were also characterized by Gordeyev et al. [12].

Active flow control approaches on turret configurations have been predominantly open-loop in nature. Numerical work by Purhoit et al. [13] predicted significant alteration of the wake structure when investigating low levels of distributed hemisphere suction. Vukasinovic and Glezer [14] demonstrated the effectiveness of fluidic, direct high-frequency control in turbulence suppression behind a bluff-body turret at $Re_D = 8 \cdot 10^5$. Vukasinovic et al. [15] simultaneously measured the aerodynamic and aero-optical environment within the separated flow off a hemispherical turret at freestream Mach number speeds up to $M = 0.64$. They reported significant suppression of turbulent fluctuations and reduction in optical distortions up to $M = 0.45$ by active flow control.

Renewed interest in the aero-optical problem of the flow over an airborne turret resulted in a number of recent investigations focused on different flow control approaches. Woszidlo et al. [10] investigated effects of passive generation of streamwise vortices in the oncoming wall boundary layer and active steady suction at the trailing-edge base on separation of the low-speed flow over the spherical protuberances. The former delayed separation off the surface, while the latter was able to remove necklace vortices around the protuberance and thereby eliminate one source of vorticity and turbulence intensity in the wake. The effectiveness of direct, small-scale control $(St_D > 10)$ of the separated flow over a hemispherical protuberance

with a thin upstream boundary layer was demonstrated by Vukasinovic et al. [9] at $Re_D = 4$–7×10^5. They showed that the presence of flow control can substantially reduce the extent of the recirculating domain downstream of the hemisphere with significant reduction in turbulent kinetic energy. Numerical work of Morgan and Visbal [16] emphasized that distributed porous suction over forward turret surface significantly delayed separation off the hemisphere at $M = 0.4$ and consequently reduced the wake extent and its turbulent intensity. Vukasinovic et al. [17] and Gordeyev et al. [18] measured both aerodynamic and aero-optical effects of synthetic jet active control of the flow over a turret, nominally at $M = 0.3$ and $Re_D = 4.5 \cdot 10^6$. It was shown that aerodynamic improvements in separation delay and suppression of turbulent energy within the wake resulted in about 30% suppression in optical aberrations as measured directly by the Malley probe. In addition to the above-mentioned open-loop control approaches, Wallace et al. [19] also presented some examples of closed-loop control effects based on the feedback from the dynamic pressure sensors over the flat aperture, which indicated further improvements upon the open-loop control approach. Finally, Gordeyev and Jumper [20] reviewed past work on the baseline and controlled flow over an airborne turret.

The present investigation builds on the findings of previous work on active control of flow over a turret by direct small-scale excitation of the flow by arrays of surface-mounted synthetic jets [17,18]. Although actuation at the frequencies comparable with the natural wake frequencies is often used in the applications aimed at a flow-separation delay over aerodynamic surfaces, there is reason to believe that excitation of the large-scale, organized motions in the wake by such a control could induce even higher optical aberrations [5] in spite of a possible favorable effect in the static (mean) sense. Therefore, actuation at the scales substantially smaller than the wake natural scales is selected, since suppression of the organized large-scale structures in the flow under such a control has already proven effective in the planar shear layers [21–23]. In addition to active flow control, the present work uses favorable global flow alterations induced by simple passive modifications of the base turret geometry. Favorable effects that are primarily manifested through the flow-separation delay via passive control are further augmented by active actuation. Simultaneous active and passive control comprise hybrid control that results in concomitant delay of flow separation and active, dissipative suppression of turbulent motions within the separated shear layer. It is interesting to note that one of the first turret flow control approaches proposed in the literature [24] is also hybrid in nature according to the definition above, as it proposed a combination of a long aft fairing (passive) and dual suction (active) control at the support surface, integrated into the fairing. While the primary objective of the current work is to assess the effectiveness of hybrid flow control for suppression of optical aberrations at $M = 0.3$, the control effectiveness was further characterized at $M = 0.4$ and 0.5. While the primary focus of this paper is on the aerodynamic effects of active and hybrid flow control, the accompanying direct aero-optical characterization is discussed in great detail in the companion paper [25]. The experimental setup and procedure are described in Sec. II. The characterization of the base flow is described in Sec. III; Secs. IV and V present the results of active and hybrid control, respectively. Finally, the conclusions are presented in Sec. VI.

II. Experimental Setup and Procedures

All experiments were conducted at the Subsonic Aerodynamic Research Laboratory (SARL) facility at Wright-Patterson Air Force Base. The SARL facility has an open-loop in-draft wind tunnel with a 2.13×3.05 m octagonal test section that is 4.57 m long. Mach number can be varied between 0.1 and 0.5. The test section was designed for a maximal optical access, having 20 eight windows built into the test-section walls, and they comprise 56% of the test-section surface area. The tunnel has a 14×15.2 m inlet, giving a 35:1 contraction ratio. Honeycomb and screens are installed in the inlet before the contraction for turbulence intensity management. The primary test-section speed for the current tests was $M = 0.3$, while

additional tests were run at $M = 0.4$ and 0.5, which correspond to Reynolds numbers $Re_D = 4.4 \times 10^6$–7.4×10^6. The turret model mounted onto the side wall of the test section is shown in Fig. 1a. It measures 0.61 m in diameter, and is equipped with a 0.254-m-diam spherical cap that models an optical window and therefore the aperture area is unavailable for the flow control hardware. During the aero-optical portion of the test [25], the instrumented cap was replaced by a full optical window with a mirror underneath. The actual laser beam reflecting out of the optical window is visualized in Fig. 1b.

A nominal turret model, shown schematically in Figs. 2a and 2b is a modified turret model previously used by Vukasinovic et al. [17] and has two major modifications as described in more detail below. The cylindrical turret base ($H/R = 0.6$) is stationary, but the central hemispherical top ($R = 0.305$ m) is fully rotational about the z axis in the turret's zenith plane, thus allowing variation in the window's elevation angle γ, which is defined as the central angular position of the window's center, relative to the horizon (freestream flow). Uncertainty in the turret positioning with respect to the elevation angle is 0.5°. The spherical top is instrumented with static pressure ports that are distributed along the central, middle (20° off centerline), and the outer (40° off centerline) planes, which include 39, 44, and 39 ports, respectively. In addition to these main pressure ports, nine static pressure ports are also distributed just upstream from the optical window, such that the middle port is in the central plane, and four pressure ports are distributed over each half of the window, having azimuthal angles $\alpha = 12.5, 25.6, 39.7$, and 57.7°. These additional nine ports are used to assess the flow symmetry and spanwise
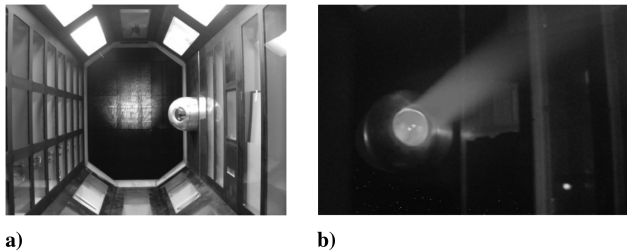
(z direction) effects of the actuation. Static pressure measurements were acquired using a Pressure Systems scanner, where average pressure measurements are typically measured over 500 individual samples, and uncertainty of the averaged pressure measurements is estimated to be less than 1%. Two main modifications of the previous turret model [17] are addition of passive flow control elements (partition plates) and surface redistribution of the active control sources. The former was motivated by the findings of active flow control of the separated flow off the hemispherical protuberance (i.e., a turret with no cylinder support) [9,15]. The latter was motivated by the findings of Vukasinovic et al. [17] that the farthest-downstream actuators that were wrapped around the optical window did not improve the aerodynamic and optical environment behind the turret. Therefore, six of those far-end actuators on each window side were redistributed to the stationary side of the turret, i.e., trunnions, as shown in Figs. 2a and 2b. The other 30 actuators were distributed in multiple rows, just upstream from the optical window, preserving the same pattern as in the previous tests. Furthermore, governed by the previous results, the current tests were done with the actuators injecting predominantly streamwise vorticity into the flow. Hence, a total of 42 individually addressable actuator modules were distributed over the turret surface. Each actuator module has a high-aspect-ratio rectangular jet orifice (measuring 38.1×0.5 mm). In addition to the actuator design, the accompanying amplifier circuitry for the actuators was also designed and built at Georgia Tech. It should be noted that no independent repositioning of the actuators relative to the optical window is allowed, as the whole hemispherical top rotates as a rigid body. This real-application requirement prompted distribution of the actuators in multiple rows, as the relative distance from the control input to the local flow-separation point varies proportionally to the turret rotation. As mentioned above, a major change in the turret geometry was done by addition of forward partition plates at the interface of the hemisphere and the supporting cylinder. Schematics of the modified turret geometry with a $R/2$ long partition plate is shown in Figs. 2c and 2d. This passive modification of the turret geometry was motivated by a desire to effect suppression of interaction between the hemisphere and cylinder wakes, as well as by generation of frontal necklace vortices that were expected to have a favorable effect on bringing the high-momentum fluid from the outer flow closer to the central zone of the turret surface. Two passive modifications of the base turret geometry were tested: the addition of forward partition plates of lengths $R/2$ and R at the point of mating of the hemisphere and the cylinder. In the present experiments, the actuation frequency was kept at $f_d = 1600$ Hz, while the actuation strength was varied over $3 \times 10^{-6} < C_\mu < 1.5 \times 10^{-5}$ per single active actuator, where the jet momentum coefficient is defined as $C_\mu = \rho U_j^2 A_j / (\rho U_0^2 A_o)$, where A_j is the total jet orifice area, A_o is the frontal projection of the turret, and U_j is the average jet velocity during the expulsion part of the cycle. It should be noted that full control using all the available actuators corresponds to the jet momentum coefficient of $C_\mu = 6.5 \times 10^{-4}$ at $M = 0.3$, which is the flow condition of primary interest.

Fig. 1   Photographs of a) turret model in the SARL tunnel and b) 25.4-cm-diam optical beam reflecting out of the turret.
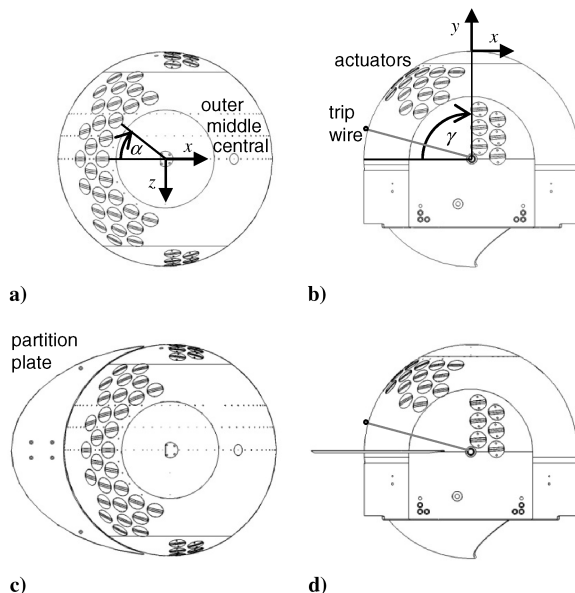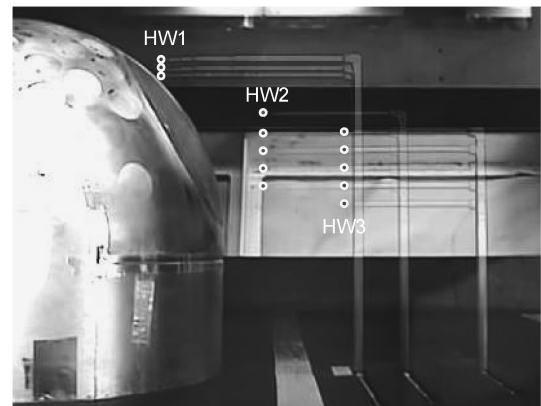

Fig. 2   Illustrations of top (left) and side (right) views of the 0.61-m-diam turret model having a 0.254 m instrumented spherical cap in place of an optical window for the nominal (top) and modified (bottom) turret geometry.

Fig. 3   Overlapped measurement positions of the three hot-film sensors downstream from the turret.

Spectral characterization of the baseline (nonactuated) and actuated flows was accomplished using single-sensor hot-film anemometry. For that purpose, three hot-film probes were mounted on retractable holders and stowed in surface wall depressions when not in use. During the measurements, only one probe at a time was elevated from the surface and positioned at the measurement location. The sensor streamwise positions are $x/R = 0.5$ (HW1), 1.1 (HW2), and 1.5 (HW3), where x is measured from the hemisphere center (Fig. 2). All the measurement locations are shown in Fig. 3, where the multiple cross-stream measurement locations were selected so that the local shear layer thickness was traversed. Hot-film output signal was sampled at 30 kHz so that the measurement resolution was about 1.8 Hz in the frequency domain. For a given flow condition, an averaged power spectrum was composed of 50 individual power spectra for suppression of random noise with 5% uncertainty.

Additional flow characterization was done by the surface oil-flow visualization, which was used to gain a better understanding of the global flow topology. The oil was applied so as to capture the flow footprint at the turret support wall, accompanied by partial visualization of the flow on the turret surface and the partition plates (when present). The flow features were educed from the series of partial snapshots of the surface oil patterns and direct measurements of the characteristic scales in the test section. The main captured features included the front and back stagnation points, a necklace vortex pattern that originates upstream of the cylindrical support, the main wake formed by the flow separation off the hemispherical top, secondary separation zones off the cylindrical support, and a partial separation line on the hemispherical top. As an illustration, several partial snapshots of the surface oil-flow visualizations are shown in Fig. 4, where localized focus is on the upstream wall stagnation area,

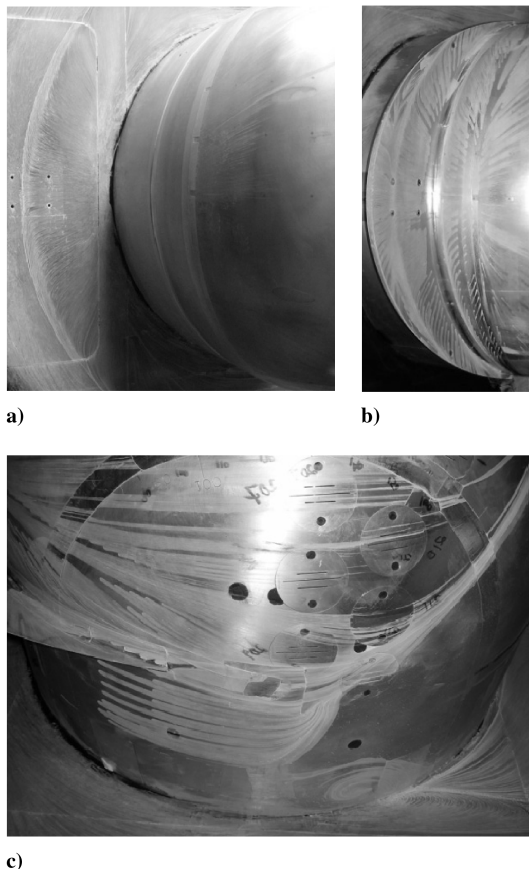a)   b)

c)

Fig. 4 Partial snapshots of the surface oil-flow visualizations illustrating a) the front stagnation point and the wall necklace vortex, b) displaced hemisphere stagnation point and necklace vortex on the partition plate, and c) separation line behind the partition plate. The flow is from left to right.

separation line on the hemispherical top, and displacement of the stagnation point on the turret due to the passive control. All such features are combined into a single schematic representation of the flow footprint for each flowfield.

III. Baseline Flow

Earlier investigations [15,17] have demonstrated that the topology of the baseline turret flow is rather complex and Mach and Reynolds number dependent. To avoid changes in separation that are associated with flow transition over the model smooth surface, the hemisphere's boundary layer in the present experiments was tripped using an overall 0.3-mm-diam wire that was placed along meridional plane at a 15° elevation relative to the center (symmetry) plane of the turret.

The resulting baseline flows are first characterized using measurements of static pressure distributions in the central, middle and outer planes (Fig. 2). The pressure profiles in these three planes are shown in Fig. 5 for window elevation angles $\gamma = 139$, 145, and 150°, and $M = 0.3$, 0.4, and 0.5. The baseline profiles for the same turret geometry [17] for $\gamma = 129$, 137, 143, and 148°, and $M = 0.3$, 0.4, and 0.5 are included in the same figure. An excellent agreement between the current and previous measurement indicates invariant baseline-flow conditions, which suggest that, for a given Mach number, the flow separates first over the outer edges of the optical window and remains attached farthest in the central plane, as the separation angles in each measurement plane nearly coincide in its own reference angles. It should be noted that the separation point is defined to be at the beginning of the profile flattening, which is expected to be correct for the open wake behind the turret. Earlier similar static pressure measurements [17] were accompanied by the seeded flow visualization in the central vertical plane in order to test such a definition of the separation point, and a good agreement between the beginning of the flattened pressure profile and the visualized point of separation was found. Clearly, resolution of such an estimate of the separation angle depends on the spacing of the static pressure ports, which in the present case yields uncertainty of 2.5°. The pressure profiles shown in Fig. 5 also indicate that the separation angle in all three planes shifts slightly upstream with increasing Mach number, such that the flow separates just upstream from 120° in the central plane at $M = 0.3$, while at $M = 0.5$, the separation point is at about $\gamma_s = 115°$. It should be noted that the baseline flow in the center zone over the hemispherical cap does not differ significantly from the flow over the upper half of the full sphere immersed into the same outer flow. Given the Reynolds number greater than 10^6 in the present experiments, the flow separation for an equivalent full sphere occurs in the supercritical regime where the boundary layer over the hemisphere is fully turbulent at the point of separation. According to Achenbach [26], the separation angle in the central plane should therefore be between 115° and 120°. Clearly, the present results for the turret with conformal aperture are in good agreement with the analogous results for the full sphere. An insight into the flow condition just upstream from the optical window is gained by the static pressure distributions over nine symmetry ports distributed along the window's upstream edge (Fig. 2). These baseline pressure distributions are shown in Fig. 6 for both the current and previous tests at $M = 0.3$ [17], and their pressure port positions comprise a full span of elevation angles of the most interest, $\gamma = 120$–150°, and also serve as a check for consistent baseline-flow conditions in both tests. In addition to a close agreement between the tests results [17] at $\gamma = 129$ and 150°, and the current $\gamma = 130$ and 150°, it is also indicative that the flow starts to separate at the outer upstream edges of the window at about $\gamma = 135°$, as the pressure level at the outmost points is just below the separation level, and that past $\gamma = 143°$ the baseline flow becomes almost fully separated over the whole optical window.

Next, the global topology of the baseline flow at $M = 0.3$ was investigated using surface oil-flow visualization. The main footprint of the flow was visualized over the flat surface of the supporting turret wall, and additional visualization was performed along the cylindrical turret base. The recorded images of the surface oil visualization
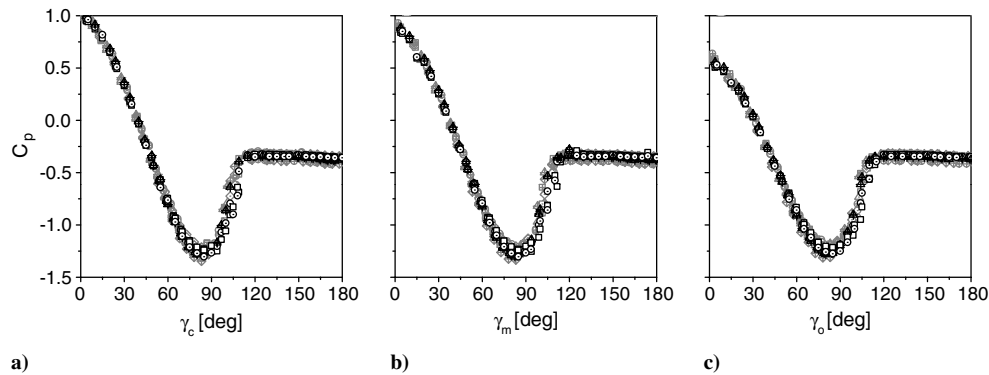
Fig. 5 Overlapped static pressure measurements at window elevation angles $\gamma = 129°$, 137, 143, and 148° (open symbols, [17]), and $\gamma = 139$, 145, and 150° (filled symbols), for the baseline flows at $M = 0.3$, 0.4, and 0.5 in the a) central, b) middle, and c) outer planes.
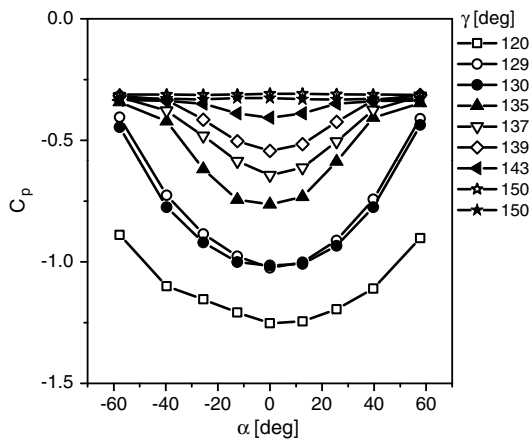

Fig. 6 Static pressure profiles upstream from the optical window for a range of turret elevation angles $\gamma = 120°$–150° and $M = 0.3$ for the current (filled symbols) and previous (open symbols) tests [17].

showed that the baseline flow over the turret is quite symmetric. Some features of the flow that were educed from these images are shown schematically in Fig. 7a (the turret support plane) and 7b (the cylinder surface). As the oncoming boundary layer approaches the adverse pressure gradient induced by the presence of the cylinder support, a spanwise (necklace) vortex is formed which becomes strained and deformed under the modified pressure field, giving a rise to the streamwise vortex branches along each spanwise edge of the cylinder. A stagnation point is formed at $0.5R$ upstream from the turret edge, and the outer flow is displaced by the bluff body, accelerates over the hemisphere surface and around the cylindrical

surface until the adverse pressure gradients on the aft sides induce separation. The flow footprints shown schematically in Fig. 7a indicate that the flow separates off the cylinder base near its apex, and spreads azimuthally by approximately 120°. The visualization on the surface of the cylinder in Fig. 7b indicates the 3-D nature of the separating flow near the cylinder base, as well as its localized, near-wall effect. Further away from the support wall, the flow trajectories over the cylinder become displaced toward the hemispherical turret cap, and merge into a separation line. This visualization supports the assessment, based on the static pressure measurements (Fig. 5), that the flow separates first at the spanwise edges of the turret and remains attached farthest in the (center) plane of symmetry. The ensuing separated flow off the turret surface has a main central wake that reattaches to the support wall at approximately $1.3R$ downstream from the turret edge and two additional near-wall vortical traces that are associated with the vortices shed off the juncture between the cylinder and the support wall. After initial narrowing, the main wake begins to spread, as shown in Fig. 7a. These visualizations indicate that the overall wake dynamics are dominated by the flow separation off the hemispherical cap, while the separation at the cylinder base has a rather localized effect on the main wake. In contrast to these findings, measurements in a high-aspect-ratio turret flow [8], where the cylindrical base is much taller than its radius, show that the near wake is dominated by the dynamics of the vortices shed off the supporting cylinder.

Spectral characterization of separated flows behind the turret was done by hot-film anemometry, as described in Sec. II. While major spectral characterization of the separated flow was done in connection with the evaluation of the flow control approaches, the baseline flow was first analyzed from the standpoint of invariant flow dynamics at different elevation angles of the turret. An example of these data at $M = 0.3$ is shown in Fig. 8, which includes three spectra of velocity fluctuations measured at $x/R = 0.5$ (HW1), 1.1 (HW2),
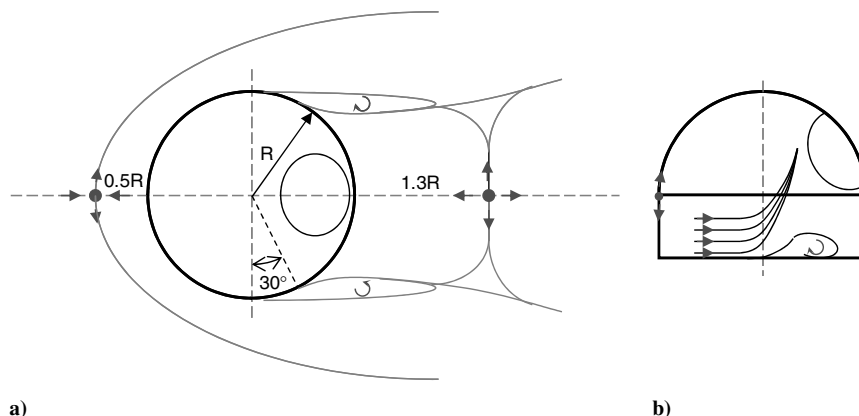

Fig. 7 Schematics of the surface oil-flow visualization of the baseline flow at $M = 0.3$ at the a) support wall and b) turret surface for the nominal turret geometry.
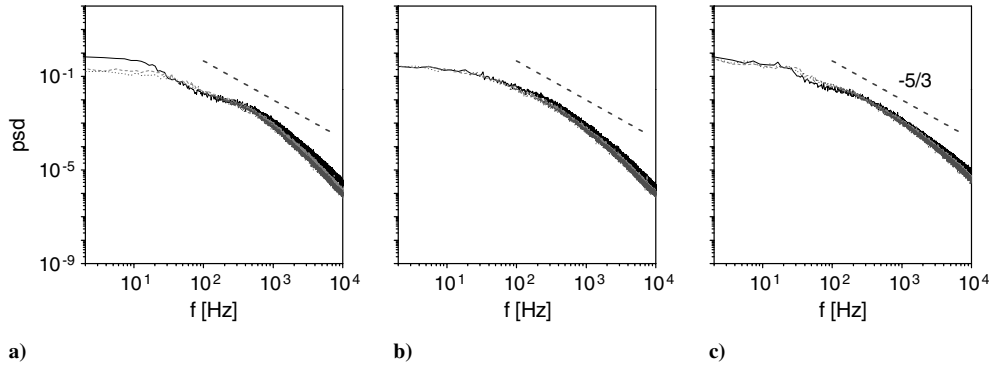
Fig. 8   Power spectra of the baseline velocity fluctuations at $M = 0.3$ **and** $\gamma = 139°$ **(solid line), 145° (dashed line), and 150° (dotted line) measured at the shear layer center at a) HW1, b) HW2, and c) HW3 locations.**

and 1.5 (HW3) at the fixed position within the shear layer, and for three elevation angles $\gamma = 139°$, 145, and 150°. These data confirm that there is no significant difference among the baseline flows, as the baseline-flow dynamics should be independent of the turret elevation angle. Some variation of energy distributions that is detected at the closest measurement station (Fig. 8a) is attributed to an error associated with the positioning of the hot-film sensor within the narrow shear layer, as it is in the case of the starting shear layer. Figure 8 also demonstrates how the inertial range of scales shifts toward the higher frequencies with an increase in downstream distance, as turbulent evolution of the flow generates motions of decreasing scales.

IV.   Active Flow Control

Figure 9 shows static pressure distributions over three measured planes (central, middle, and outer, Fig. 2) for the baseline and controlled flows at $M = 0.3$, 0.4, and 0.5. In addition, the corresponding pressure profiles [17] for the controlled flow under the same conditions at $M = 0.3$ and 0.4 but different distribution of the actuator modules (as described in Sec. II), are shown as a reference. As flow control is activated, there is an almost identical effect measured in all three planes at $\gamma = 139°$ (Figs. 9a–9c). The flow separation becomes delayed by $\Delta\gamma_s > 10°$ and, contrary to previous tests [17], this effect does not weaken across the span. Such extended effect in the spanwise direction relative to the previous tests [17] is attributed to the spatial redistribution of actuators, which also populate the turret sides in the present tests (Figs. 2c and 2d). As the Mach number is increased to $M = 0.4$ (Figs. 9d–9f), a substantial separation delay is sustained upon actuation in the central plane, with some weakening toward the outer planes. Finally, at the highest Mach number $M = 0.5$ (Figs. 9g–9i), nearly uniform but weak separation delay is achieved across the optical window area. Overall, redistribution of the control actuators to the turret sides showed consistent improvement in separation delay, when compared with the previous test [17]. These findings are also in accord with the conclusions drawn from the turret control at lower speeds [14], which explored the effect of varying spanwise extent of the control sources.

For all the baseline flows tested ($M = 0.3$–0.5), the shape of any baseline pressure distributions upstream from the optical window evolves in a similar manner with the elevation angle, as shown in the most detail in Fig. 6 for $M = 0.3$. They clearly indicate that the flow begins to separate first at the outer edges of the optical window, while the upstream central zone of the window is traversed by the still-attached flow. Static pressure distributions just upstream of the optical window edge are shown in Fig. 10, corresponding to the test cases of Fig. 9. As flow control is activated, significant acceleration of flow around the turret is induced, manifested by a pressure drop across the window upstream edge. Consequently, this effect would enable flow to remain attached further in the streamwise direction. This favorable effect on flow separation is pronounced strongly in the central zone of the optical window, with some weakening in the outward direction. Furthermore, as also seen in Fig. 9, the separation

delay becomes less pronounced with increase in Mach number as the control is effected at a fixed control jet output, which effectively decreases its momentum coefficient as the momentum of the outer flow is increased. It should be noted that comparable results from previous tests [17] show that favorable effect of flow control completely vanished at the outer edges of the window ($\alpha \approx \pm 60°$). The current results show that there is an increase in the pressure drop across the optical window span relative to the corresponding actuation before the actuator redistribution [17]. Such a favorable flow acceleration upstream from the optical window is attributed to redistribution of the actuators and their presence along the cylinder sides, which is known to enhance the overall flow control effect [14]. Furthermore, it appears that the current flow control approach also enhances separation delay at both $M = 0.3$ and 0.4, when compared with the previous tests [17].

In addition to the nominal actuation approach where all of the jets are used at the highest jet momentum coefficient (case AC1), additional tests were done to test how different spatial distributions of actuators affect the flow control and how varying jet momentum coefficient affects the flow control effectiveness. The former is done by rendering two side clusters of actuators inactive (AC2), see Fig. 2, and by the flow control exclusively by the band of actuators closest to the optical window (AC3). The next test was facilitated by a full set of actuators having the actuator strength lowered below the nominal level (AC4), and lowered even further (AC5). Static pressure profiles corresponding to the baseline flow at $\gamma = 139°$ and these five actuation scenarios are shown in Figs. 11a–11c for the central, middle, and the outer measurement planes, respectively. As seen in these plots, separation delay is directly proportional to both the actuation strength and population of the actuation sources. These results are in accord with previous similar tests on similar geometries [14,17]. Based on the profiles that result from the actuation cases AC1-3, it can be concluded that exclusion of side actuators has a less detrimental effect on flow-separation delay than exclusion of the second row of actuators upstream from the optical window. The weakening of separation delay with weakening of the jet strength has already been proven in both low-speed [14] and high-speed [15] tests, and current results support those findings. It is interesting to note, however, that the weakest actuation at the full set of actuators (AC5) is still preferable than actuation at full strength by a significantly reduced number of actuators (AC3). Accompanying static pressure distributions over the front border of the optical window are shown in Fig. 11d, and these profiles suggest that the principal effects seen in the three representative planes (Figs. 11a–11c) are a true representative of the full spanwise effects over the optical window, since a family of inverted bell-shaped profiles follow the same trends discussed in conjunction with Figs. 11a–11c.

Next, the use of active flow control was tested at three turret elevation angles, $\gamma = 139$, 145, and 150°, and $M = 0.3$. Resulting static pressure profiles measured in three planes: central (symmetry plane), middle (20°-off central), and outer (40°-off central) are shown in Fig. 12 for the baseline flow (open symbols) and controlled flow by the full set of actuators (filled symbols). Baseline profiles indicate, as
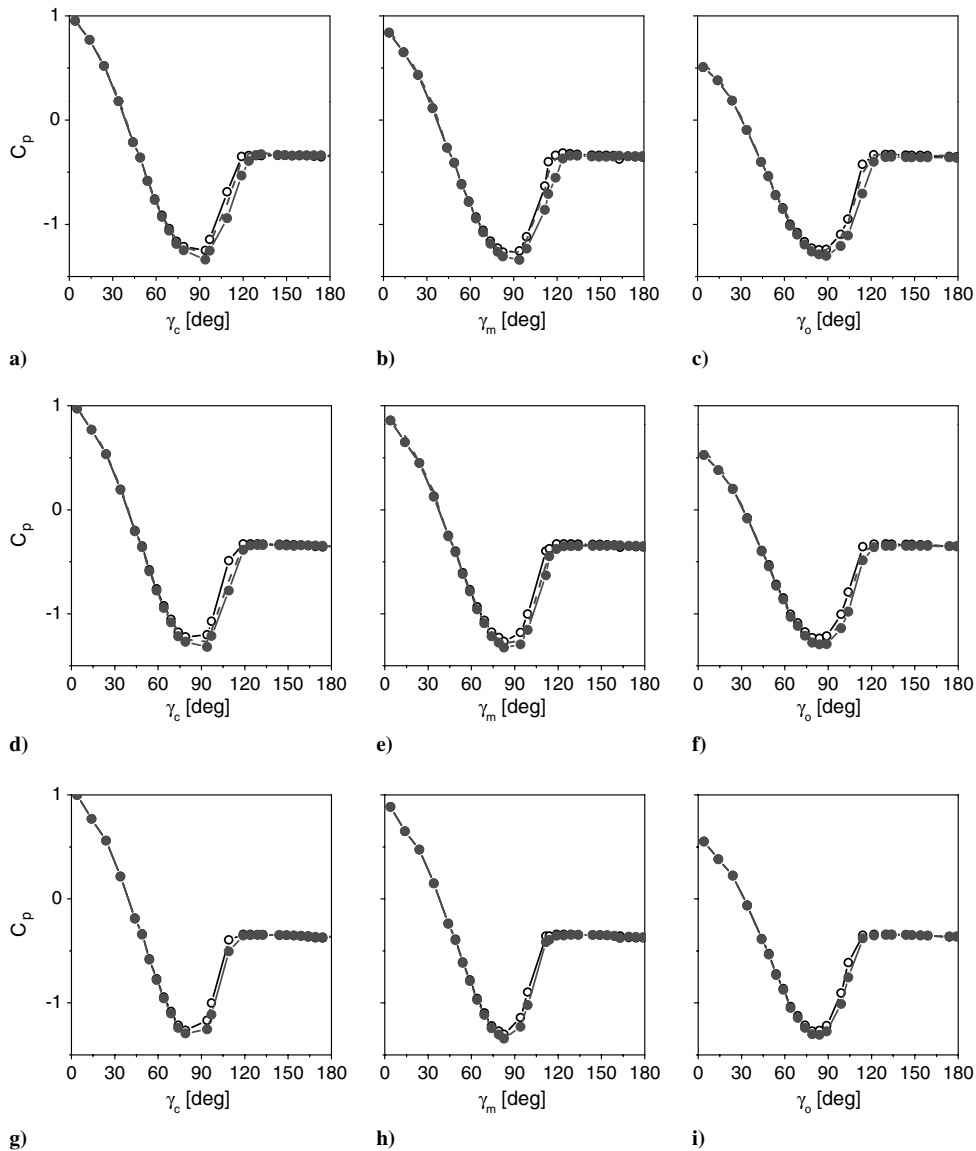
Fig. 9   **Static pressure profiles at the window elevation angle $\gamma = 139°$ and $M = 0.3$ (a–c), 0.4 (d–f), and 0.5 (g–i) in the central (left), middle (middle), and the outer (right) planes for the baseline (open circle) and the flow actuated by full actuation (filled circle). The corresponding results (dashed line [17]) for the actuated flow are also shown as a reference.**

expected, a stagnation point ($Cp = 1$) at zero incidence in the central plane and nonzero, increasing velocities toward the outer plane ($Cp < 1$). Also, as the flow accelerates toward the turret apex, local velocities there ($\gamma_{c,m,o} = 90°$) are nearly identical. The effects of the

flow control at $\gamma = 139°$ are already discussed in conjunction with Fig. 9. The strong separation delay seen at this elevation angle (Figs. 12a–12c) is sustained at $\gamma = 145°$ (Figs. 12d–12f), while a somewhat smaller separation delay is measured at the highest
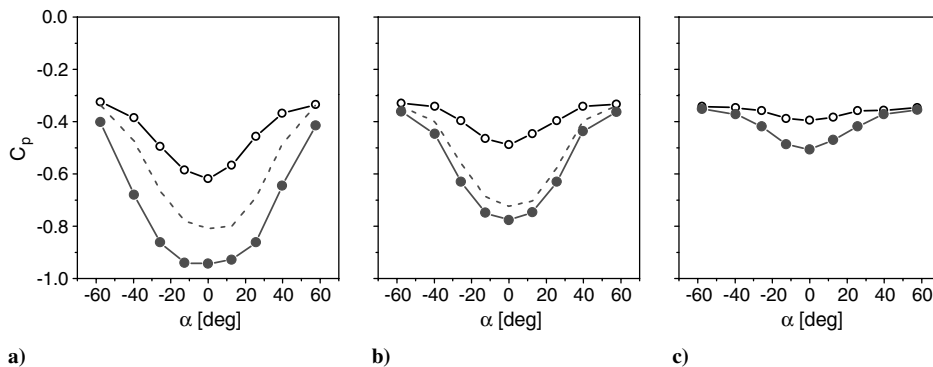

Fig. 10   **Pressure distributions about the optical window center ($\alpha = 0°$) at window elevation angle $\gamma = 139°$ for the baseline flow (open symbols) and the actuated (closed symbols) flow at a) $M = 0.3$, b) 0.4, and c) 0.5. The corresponding results (dashed line [17]) for the actuated flow are also shown as a reference.**
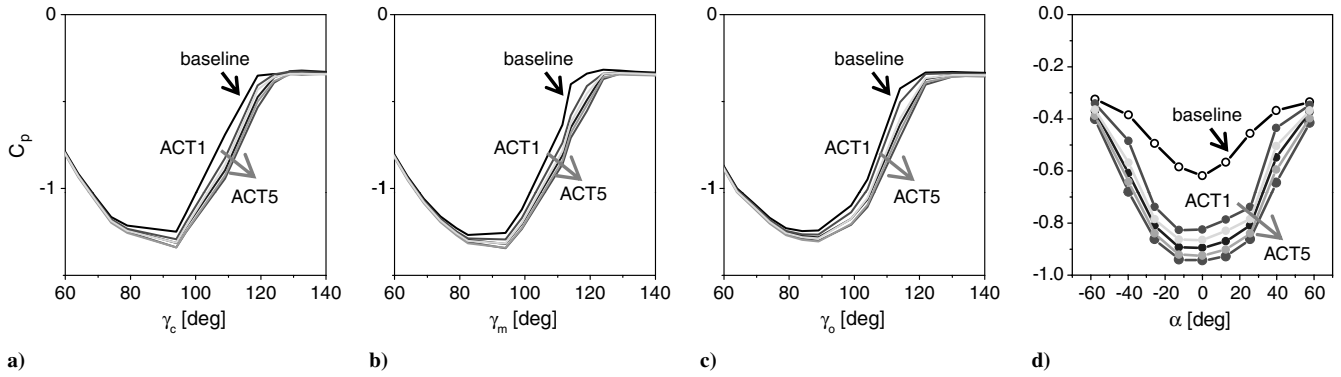
Fig. 11 Static pressure profiles in the a) central; b) middle; c) outer planes for the baseline and actuated flows at $M = 0.3$ and $\gamma = 139°$, by ACT1, ACT2, ACT3, ACT4, and ACT5; and d) corresponding pressure distributions around the optical window.

elevation angle $\gamma = 150°$ (Figs. 12g–12i). Overall, the separation delay indicates that the flow control effect in the present tests has more favorable effect on mitigation of flow separation over the optical window than in the previous test [17], which is attributed to redistribution of ineffective control elements to the turret sides, thus effectively increasing the spanwise extent of control elements.

Further analysis of the control effect is based on the static pressure distributions just upstream of the optical window, which are shown in Fig. 13, corresponding to the test cases of Fig. 12. As already discussed with respect to Fig. 10, the shape of the baseline pressure distribution at $\gamma = 139°$ (Fig. 13a) clearly indicates that the flow separates first at the outer edges of the optical window, and that the
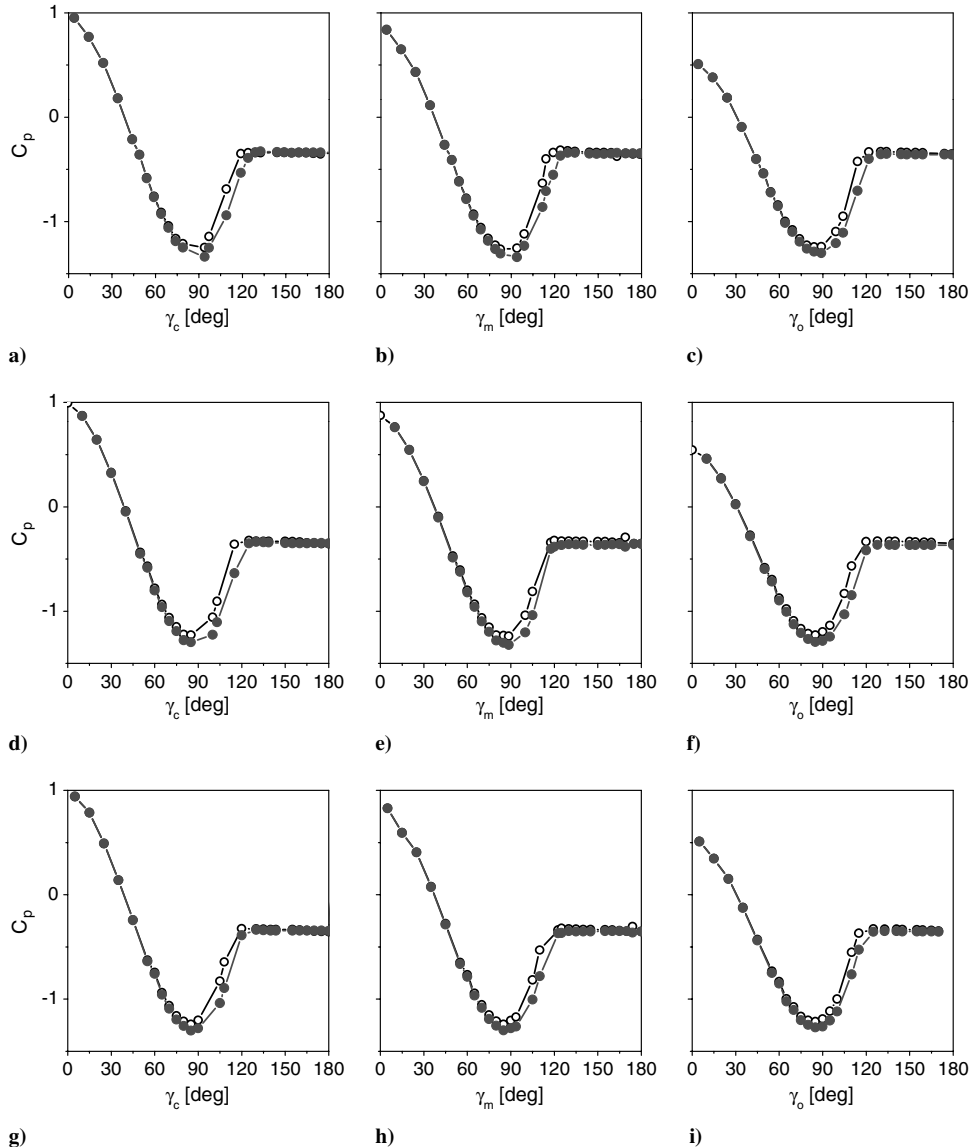

Fig. 12 Static baseline pressure profiles at the window elevation angle at $M = 0.3$ and a–c) $\gamma = 139°$, d–f) 145°, and g–i) 150° in the central (left), middle (middle), and the outer (outer) planes for the baseline (open circle) and the flow actuated by full actuation (filled circle).
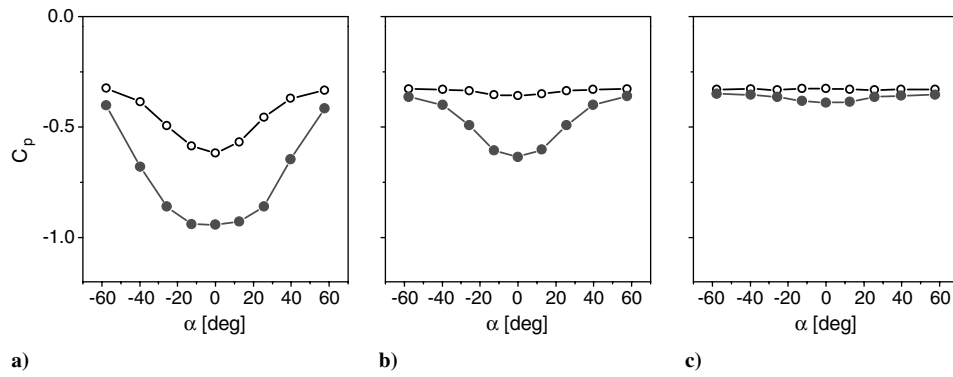
Fig. 13 Pressure distributions about the optical window center ($\alpha = 0°$) at $M = 0.3$ and window elevation angle a) $\gamma = 139°$, b) 145°, and c) 150° for the baseline flow (open circle) and the actuated (filled circle) flow.

upstream central zone of the window is traversed by the still-attached flow. As the flow control is activated, a favorable effect of the flow-separation delay is pronounced strongly in the central zone of the optical window, with some weakening in the outward direction. At the next elevation angle, $\gamma = 145°$ (Fig. 13b), the flow is almost fully separated at the measurement locations upstream from the optical window. Upon the activation of flow control, the nonseparated flow

condition is recovered upstream from the window border, as evidenced by the pressure dip. The inverted bell shape suggests again that the control effect is strongest at the central zone of the window, and that it weakens in the outward direction. Still, some effect is seen again even in the most-outward measurement location, which was not the case in the previous active control tests [17]. The baseline flow is fully separated at the highest elevation angle $\gamma = 150°$ (Fig. 13c),

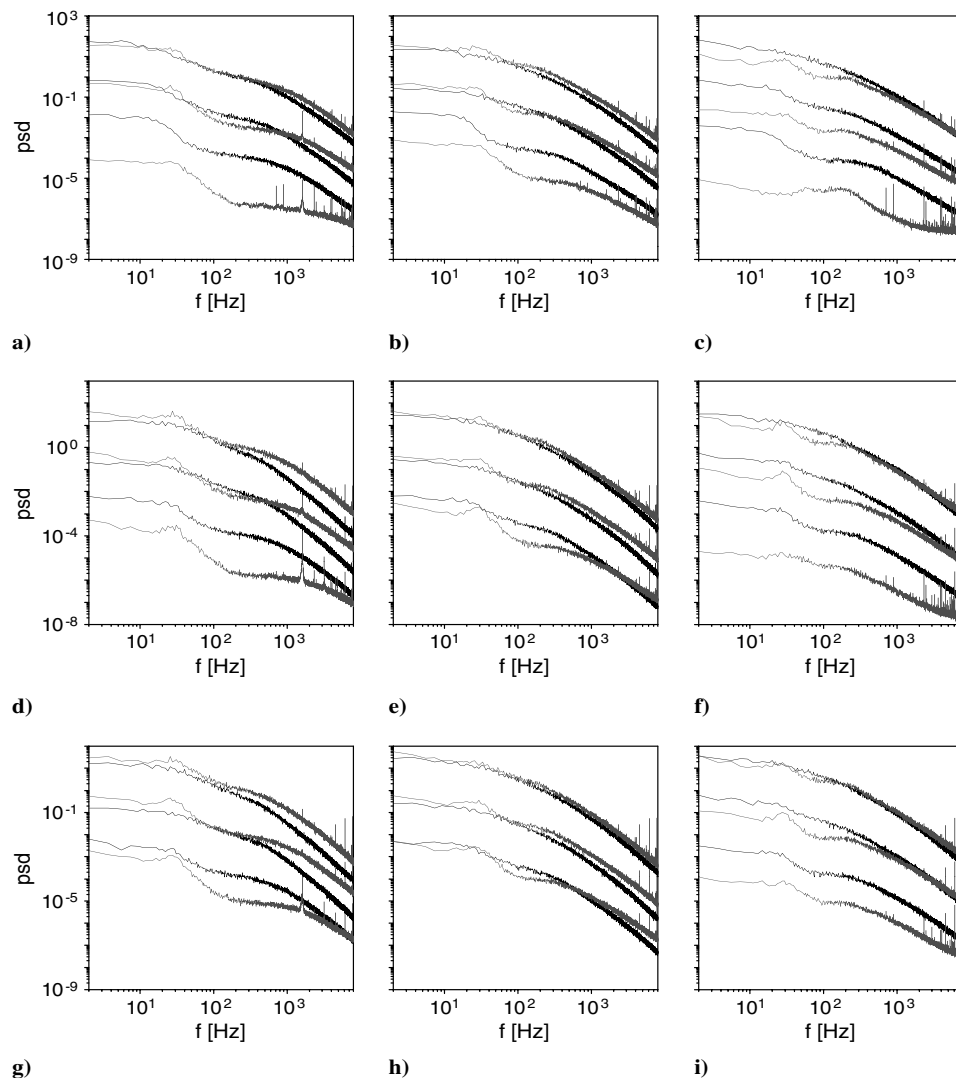**Fig. 14 Power spectra of the velocity fluctuations ($M = 0.3$) for the baseline (black) and actuated flow at a–c) $\gamma = 139°$, d–f) 145°, and g–i) 150° measured by the HW1 (left), HW2 (middle), and HW3 (right) at the high-speed edge (lowest pair), center (middle pair), and low-speed edge (highest pair) of the shear layer. Pairs of spectra for the center and low-speed edges are offset by two and four decades, respectively.**
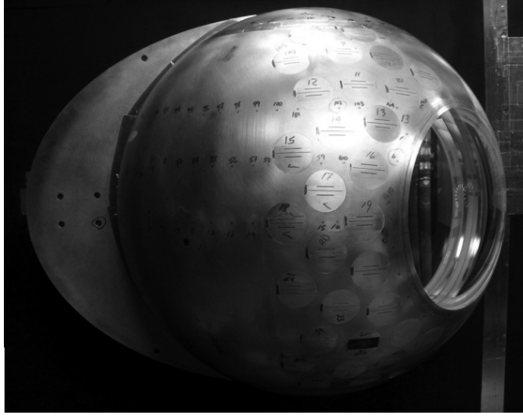
a)
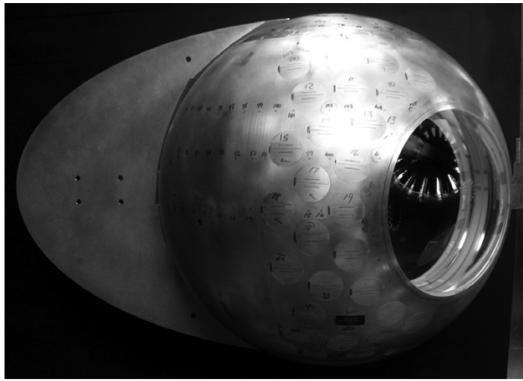
b)

Fig. 15   Passive modifications of the base turret geometry by addition of the forward a) short and b) long partition plate.

and that appears to be the most difficult case for maintaining the nonseparated flow over at least part of the optical window. The flow control still improves the flow state, but recovers only a nearly separated-flow condition upstream from the window. Overall trends in the results of the flow control measured in the current tests are in accord with the previous tests, at both low-speed [14] and high-speed [15] tunnel speeds, and they suggest that optimal flow control source positioning is just upstream from the local separation. However, application-oriented distribution of control sources limited a real estate available for the distribution of actuators. Furthermore, their continuous rotation relative to the separation line with rotation of the optical window results in a more preferable relative positioning of the actuators at lower elevation angles γ, and less preferable relative positioning of the actuators at higher elevation angles.

In addition to a static (mean) flow control effect on the base turret geometry that was discussed above, characterization of the flow dynamics was done in the spectral domain using the single-sensor hot-film anemometry. Hot-film measurements were done at three downstream locations HW1, HW2, and HW3, as described in Sec. II. As an illustration of flow control effect on the shear layer, velocity fluctuation spectra are shown for the baseline and the actuated flows in Fig. 14 for $M = 0.3$ and $\gamma = 139°$, 145, and 150°. Three power spectra for the baseline and actuated flows are shown for each γ and at each downstream measurement position, where the bottom pair of spectra corresponds to the high-speed edge of the shear layer, the middle pair corresponds to the shear layer bulk (and is offset by 10^2 in magnitude for clarity), and the upper pair corresponds to the low-speed edge of the shear layer (and is offset by 10^4 in magnitude for clarity). Similar effects are seen at all elevation angles. A typical near-field effect of actuation is seen at both HW1 (Figs. 14a, 14d, and 14g) and HW2 (Figs. 14b, 14e, and 14h) positions: significant broadband reduction in fluctuating energy is measured over the high-speed edge of the shear layer, and increase of the energy at small scales and concomitant decrease of energy at the large scales is detected within the shear layer bulk. Furthermore, predominantly an increase in energy is detected along the low-speed edge of the shear layer. At the farthest-downstream measurement location (Figs. 14c, 14f, and 14i), suppression of energy over the large-scale motions dominates each spectra, regardless of the elevation angle. Also, as the control sources are moved downstream with the increase in elevation angle, some increase in energy of the small scales becomes prominent with an increase in γ.

V.   Hybrid Flow Control

Hybrid flow control applied in this work is composed of passive flow control by addition of a forward partition plate to the base turret geometry in addition to the active flow control that is already described in Sec. IV. A motivation for addition of the forward partition plate came from the previous flow control tests on the hemispherical turret, i.e., a hemispherical shell on a horizontal support wall [9]. The main flow feature present in a baseline flow over the hemispherical, but not in the hemisphere-on-cylinder turret, is a formation of the necklace vortices at the front stagnation zone of the hemisphere. These necklace vortices have a potential twofold favorable effect on the flow-separation delay: they effectively displace the stagnation point downstream from the horizon, and have a predominantly downwash motion toward the hemisphere center. They also have a potentially detrimental effect on turbulence intensity in the wake, because they constitute an additional vorticity source that merges with the main wake. Therefore, addition of the forward partition plate is designed to emulate a presence of the support wall, as in the hemispherical turret geometry. To test this approach, two passive modifications of the base turret geometry were tested: the addition of 15.2 and 30.4 cm long forward partition plates
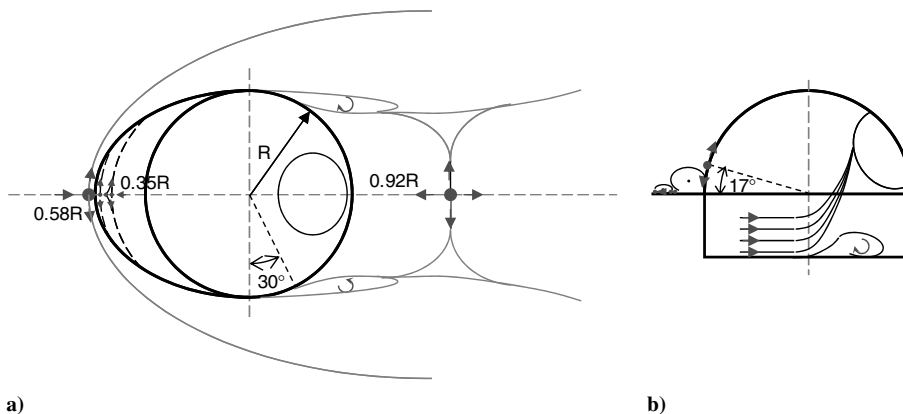
a)   **b)**

Fig. 16   Schematics of the surface oil-flow visualization of the baseline flow at $M = 0.3$ at the a) support wall and b) turret surface for the turret with a short forward partition plate.
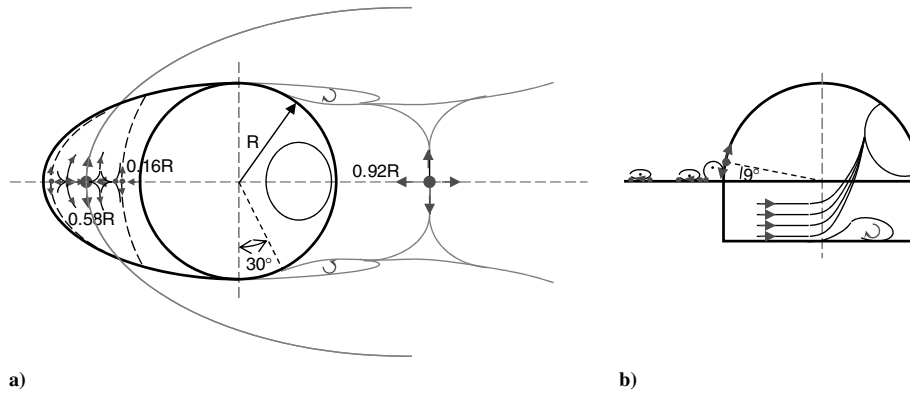
Fig. 17 Schematics of the surface oil-flow visualization of the baseline flow at $M = 0.3$ at the a) support wall and b) turret surface for the turret with a long forward partition plate.

at the point of mating of the hemisphere and the cylinder. The resulting modified turret geometries are shown in Fig. 15. It should be noted that addition of an aft partition plate was also tested in low-speed tests [14], in which case the plate's role is shifted, acting as a splitter between the wakes forming off the hemisphere and off the cylindrical support.

First, the resulting baseline flows (without the active flow control) are characterized in order to gain a better understanding of the impact that only a passive control surfaces have on the ensuing separated flow. Altered global flow topology is assessed from the surface oil-flow visualization, which is already presented for the base turret geometry (no passive modifications) in Fig. 7. Significant impact on
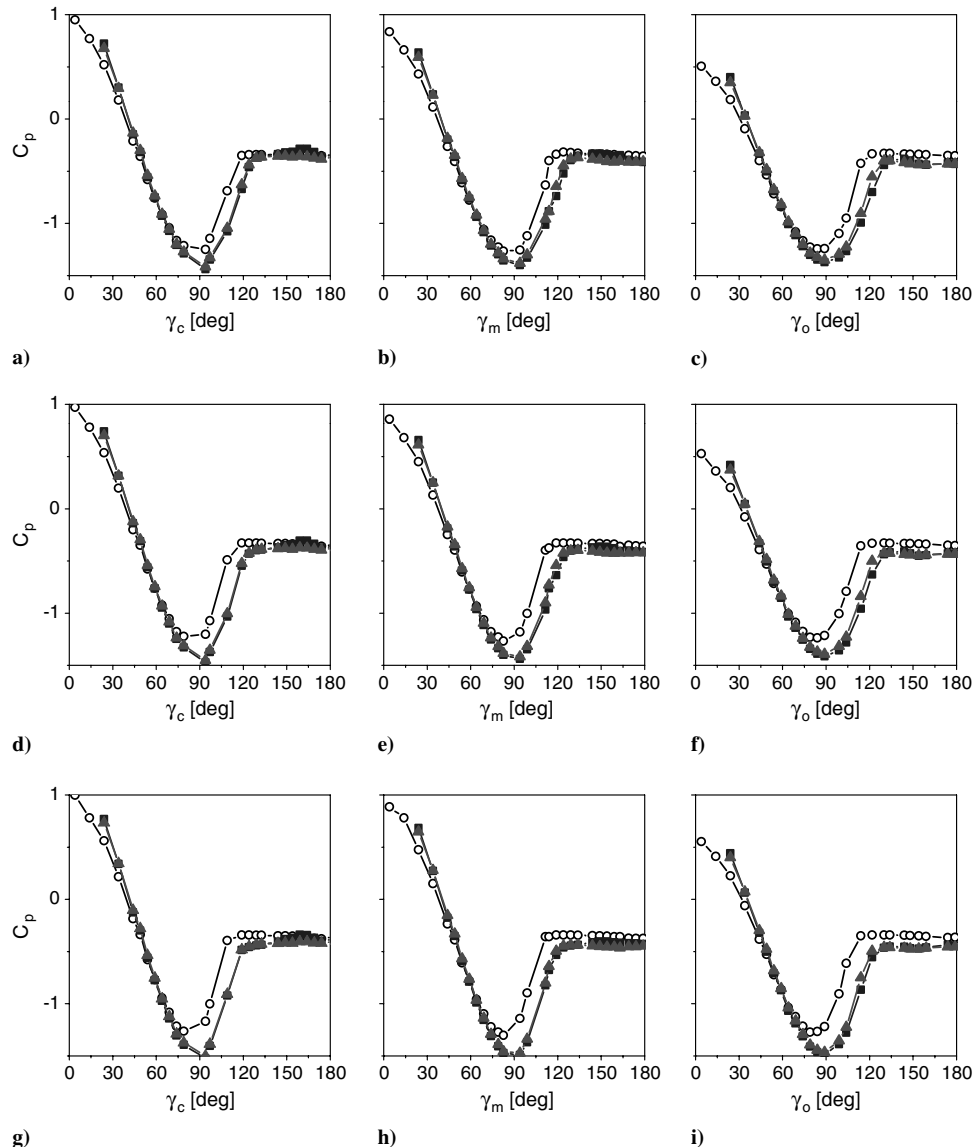

Fig. 18 Static baseline pressure profiles at the window elevation angle $\gamma = 139°$ and a–c) $M = 0.3$, d–f) 0.4, and g–i) 0.5 in the central (left), middle (middle), and outer (right) planes for the base turret geometry (circle) and added short (square) and long (triangle) forward partition plate.

the flow topology is seen in Fig. 16, when the shorter forward partition plate is added to the base turret geometry. Two major differences are seen relative to the baseline topology at $M = 0.3$ (Fig. 7). First, the flow remains attached farther over the hemispherical surface, i.e., the separation line is pushed downstream (Fig. 16b), such that the flow remains attached over the most upstream portion of the optical window. Second, once separated, the flow reattaches to the support wall closer to the model, at about $0.92R$ downstream from the model edge. Secondary separation off the cylinder base becomes altered too, as the main separated zone spreads even more across the span, and measures $1.83R$ at its throat. A presence of the plate also clearly modifies the initial interaction region between the oncoming flow and the turret. The wall stagnation point becomes displaced farther upstream at $0.58R$, while the major alteration is observed at the front stagnation region at the turret surface (Fig. 16a). Presumably due to the finite plate thickness, the flow separates off the leading edge of the plate, and as soon as it reattaches to the plate it separates again at about $0.35R$ upstream from the hemisphere due to the pressure modified by the hemispherical body that induced formation of a necklace vortex around the hemispherical cap. This modified stagnation zone in front of the hemispherical cap displaces the stagnation point on the body to about $17°$ relative to the horizon (Fig. 16b), and creates the vortex that eventually opens around the body. All the main features of the flow dynamics described due to the presence of the partition plate can be seen in the visualization snaphot shown in Fig. 4c. As the outer speed increases to $M = 0.4$ (not shown), all major features described above for $M = 0.3$ are present, with some length-scale alterations: the necklace vortices around the hemispherical cap become narrower, i.e., spread about $0.31R$ upstream from the cap, while the reattachment point of the wake moves even closer to the turret at $0.83R$ downstream from the turret edge. As already stated, the baseline wake over the nominal turret geometry at $M = 0.4$ reattaches at $1.92R$. Hence, addition of the shorter forward plate results in over a 50% reduction in the wake length. Note that the corresponding reduction in the wake extent is about 30% at $M = 0.3$, i.e., a higher wake suppression is achieved at higher Mach number.

A global flow topology does not change much at $M = 0.3$ if a longer partition plate is placed instead of the shorter one, as seen in the schematics shown in Fig. 17. Virtually nothing changes besides the approach stagnation zone to the hemispherical surface. The longer plate enables a fuller flow evolution over its surface, once the approaching flow separates off the leading edge of the plate. The flow first reattaches to the plate surface, and then forms a double stagnation zone in front of the hemispherical cap, similar to the double front stagnation at the support wall for the base turret geometry at $M = 0.4$. The inner recirculating zone measures about $0.16R$ in the central cross section (less than the corresponding one at the short plate) and opens around the hemispherical cap. As a consequence, the stagnation point at the hemispherical surface is now less displaced relative to its displacement with the shorter plate, to about $9°$ (Fig. 17b). As the outer speed is increased to $M = 0.4$ (not shown), the central reattachment point of the wake becomes slightly pushed downstream to about $1.04R$, which represents more than a 45% reduction of the wake length than in the corresponding baseline flow over the nominal turret geometry (without any partition plate).

Similar effects of both partition plates on the baseline flow are also seen in the static pressure profiles along the central, middle, and outer measurement planes. Figure 18 shows these profiles for the base turret geometry and passive modifications including both partition plates at $\gamma = 139°$ and $M = 0.3$, 0.4, and 0.5. Regardless of the pressure plane or even a Mach number, a significant favorable alteration of the baseline flow around the turret is measured after the addition of either partition plate. This alteration of the baseline flow is primarily manifested through significant separation delay of more than ten degrees in any of the measured planes. The second significant feature of the altered pressure profiles implies a strong acceleration of the outer flow around the turret, as pressure levels decrease notably starting at about $\gamma_{c,m,o} = 70°$. Not only that the favorable effect does not diminish in an outward direction across the optical window, but it appears that the favorable effect becomes even more pronounced (e.g., compare Figs. 18a and 18c). The third alteration of the baseline profiles is manifested at the very upstream
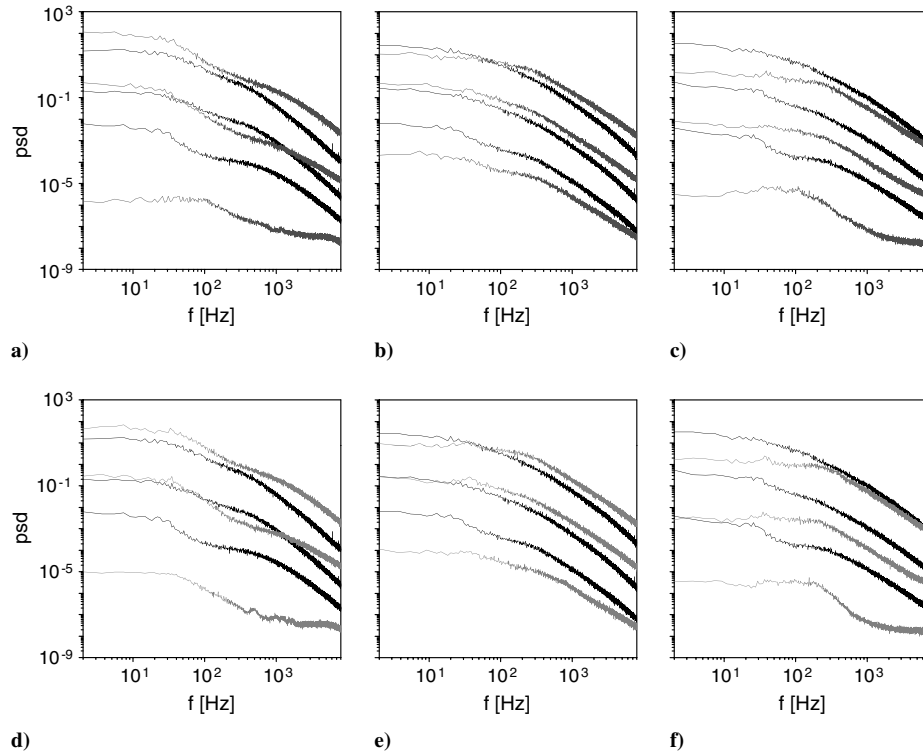

Fig. 19 Power spectra of the baseline-flow velocity fluctuations ($M = 0.3$) for the base turret geometry (black) and modified geometry with forward a–c) short and d–f) long partition plates at $\gamma = 145°$ measured by the HW1 (left), HW2 (middle), and HW3 (right) at the high-speed edge (lowest pair), center (middle pair), and low-speed edge (highest pair) of the shear layer. Pairs of spectra for the center and low-speed edges are offset by two and four decades, respectively.

end of the hemispherical cap, where the displaced stagnation point on the hemispherical surface increases the local static pressure. In addition to these three major effects, it should be emphasized that the favorable effect on the flow does not diminish with the increase in the freestream Mach number from $M = 0.3$ to 0.5. These finding suggest that the present passive modifications of the base turret geometry would induce a significant flow-separation delay even beyond the range of freestream speeds under investigation, i.e., for $M > 0.5$. Additional static pressure measurements at two other elevation angles (not shown) just confirm invariance of the baseline flow over the turret with partition plates, as the baseline flows do not depend on the optical window elevation angle.

The next characterization of the passive control effect relative to the base turret geometry was done in the spectral domain using single-sensor hot-film anemometry, analogous to characterization done for active flow control, shown in Fig. 14. Hot-film measurements were done at three downstream locations, HW1, HW2, and HW3, as described in Sec. II. As an illustration of the partition-plate effect on the separating-flow shear layer, velocity fluctuation spectra are shown in Fig. 19 for the base turret geometry and added short and long partition plates at $M = 0.3$ and $\gamma = 145°$. Each plot shows three pairs of spectra, where the bottom pair corresponds to the high-speed edge of the shear layer, the middle pair corresponds to the shear layer bulk (and is offset by 10^2 in magnitude), and the upper pair corresponds to the low-speed edge of the shear layer (and is offset by 10^4 in magnitude). Resulting spectra seem virtually independent of the partition-plate size, as energy distributions are both in qualitative and quantitative agreement. Therefore, it is suggested that the central wake dynamics are not sensitive to the selection of a partition plate. In either case, near-field dynamics (Figs. 19a and 19d) shows significant broadband reduction in the fluctuating energy over the high-speed edge of the shear layer, an increase of the energy at both the small and large scales, with some suppression in the midrange within the shear layer bulk, and mostly broadband increase in energy along the low-speed edge of the shear layer. These characteristics reflect postponed separation and the fact that shear layer is drawn closer to the turret surface, as already surmised from pressure profiles (Fig. 18) and surface oil-flow visualization (Figs. 16 and 17). Further downstream (Figs. 19b and 19e), lowered broadband suppression at the high-speed edge is accompanied by a smaller increase in energy in the bulk and along the low-speed edge, where some decrease of energy is still measured at the largest scales. Finally, at the farthest-downstream measurement location (Figs. 19c and 19f), suppression of energy over large-scale to broadband motions dominates each spectrum, regardless of the cross-stream position. Spectral results for different elevation angles are omitted, as they only show invariance in the flow dynamics with the elevation angle change.

Figure 20 demonstrates the incremental effects of passive and hybrid (simultaneous passive and active) flow control relative to the base turret geometry and pure active flow control on the mean flow upstream from the optical window. Static pressure distributions just upstream from the turret optical window are shown for $M = 0.3$ and three elevation angles, $\gamma = 139, 145$, and $150°$, with and without partition plates, and with and without active flow control. At the lowest elevation angle (Figs. 20a and 20b) pure active flow control has the strongest impact among all elevation angles. Passive addition of either plate delays the separation even more, as evidenced by the additional pressure drop. Furthermore, the passive flow control effect is more evenly distributed over the optical window span. Upon activation of hybrid flow control an extra additive effect of the active flow control is seen in further favorable preconditioning of the flow upstream from the optical window. At the next elevation angle (Figs. 20c and 20d), a similar but weaker effect is seen in both the passive and hybrid flow control. Presumably, the most important effect is seen at the highest elevation angle (Figs. 20e and 20f), where the flow over the base turret geometry is fully separated upstream from the optical window. Passive and hybrid flow control are capable of fully recovering the nonseparated flow condition upstream from the optical window, which were shown to have significant ramification of suppression of the optical aberrations even at this most-

backward-looking angle [25]. In comparison of short and long partition plates as components in the hybrid flow control, it should be also emphasized that regardless of the plate used, hybrid flow control results are almost identical. This stems from the fact that if the effect of passive control is weaker, the active part of the hybrid control yields a stronger increment, and vice versa (see, for example, Figs. 20e and 20f).

Therefore, either passive modification of the base turret geometry induces larger separation delay than in the case of active flow control on the base geometry. Further outer flow acceleration measured in further reduction of the mean surface pressure is achieved when the active flow control is applied to the modified turret geometry. It should be also noted that static pressure profiles reflect only a static component of the active flow control effect on the flow that is expressed through the separation delay—active suppression of the large-scale motions in the wake are assessed by supplemental diagnostics, such as the hot-film and direct optical measurements.

Similar to the characterization of the impact on the shear layer dynamics between baseline and passive flow control at $\gamma = 145°$
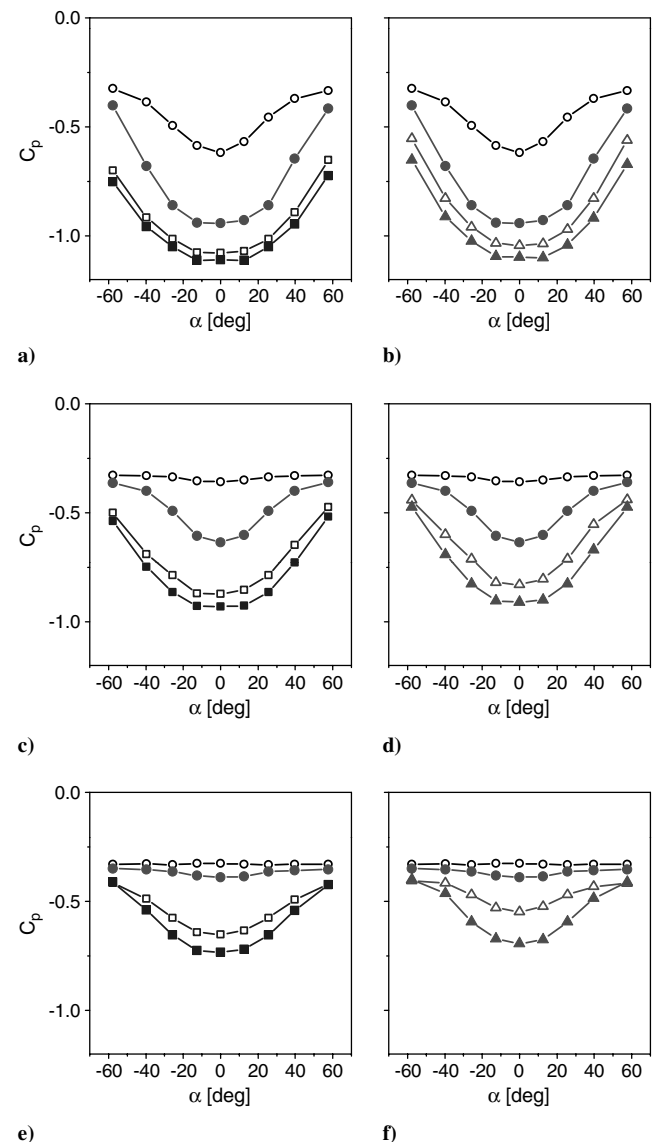

Fig. 20   Static pressure distributions about the optical window center ($\alpha = 0°$) at $M = 0.3$ and the window elevation angles a–b) $\gamma = 139°$, c–d) $145°$, and e–f) $150°$ for the baseline (open circle), active (filled circle), passive [short (open square) and long (open triangle) forward partition plates], and hybrid [short (filled square) and long (filled triangle) forward partition plates] flow control.
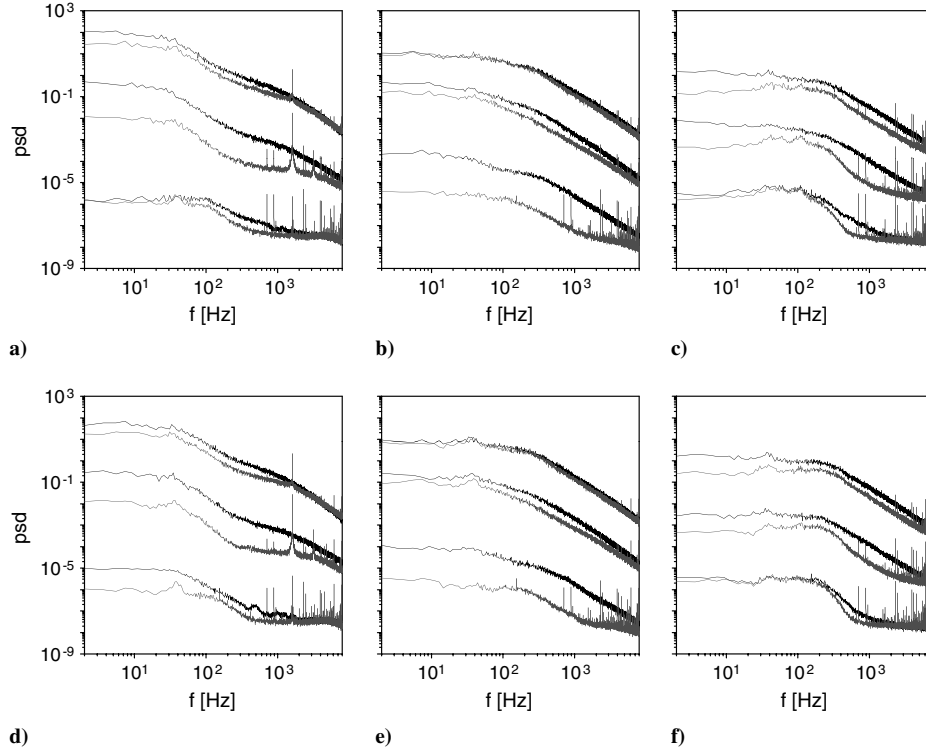
Fig. 21   Power spectra of velocity fluctuations ($M = 0.3$) for passive (black) and hybrid control of the modified turret geometry with forward a–c) short and d–f) long partition plates at $\gamma = 145°$ measured by the HW1 (left), HW2 (middle), and HW3 (right) at the high-speed edge (lowest pair), center (middle pair), and low-speed edge (highest pair) of the shear layer. Pairs of spectra for the center and low-speed edges are offset by two and four decades, respectively.

(Fig. 19), difference in spectral content of the hybrid and passive flow control is assessed from the analogous measurements shown in Fig. 21. It is significant that the hybrid flow control results in an overall suppression in broadband energy of velocity fluctuations, regardless of either streamwise or cross-stream measurement position. Furthermore, with some minor differences, the effect is quite similar at $\gamma = 150°$ (not shown), which indicates spatial robustness of the active flow control. Much as the static pressure distributions in Fig. 20, comparison of spectral properties of the shear layers in Figs. 14, 19, and 21, suggests even more that there is a clear advantage of the hybrid flow control over passive and active control in overall suppression of turbulent fluctuations in the shear layer separating off the turret.

Finally, an illustration of the resulting aero-optical effect of the hybrid flow control is shown in Fig. 22. A detailed presentation of the accompanying aero-optical flow diagnostics is done by Gordeyev

et al. [25]. Here, only the flow control effect is shown in terms of a Strehl ratio SR, i.e., ratio of the laser beam intensity at the detection plane to the theoretical maximum intensity of a perfect imaging system working at the diffraction limit. It is calculated using the large aperture approximation and a $\lambda = 1$ μm laser wavelength as SR= $\exp(-(2\pi \cdot \text{OPD}_{\text{rms}}/\lambda)^2)$, where the spatial root-mean-square of the beam's optical path difference OPD_{rms} is measured by the 2-D wave-front sensor at $M = 0.3$. First, it should be noted that, similarly to the aerodynamic characterization, no significant difference is seen between the short and long partition plates as passive components in the hybrid control. Measurement at the lowest elevation angle and short passive plate indicates a decrease in SR relative to the baseline, and it may be attributed to the excessive active control (kept constant for all elevation angles) at this angle, for which even the baseline SR is very high. Next, it is interesting to note that using hybrid control, nearly invariant Strehl ratio is achieved for all higher elevation angles, at SR ≈ 0.8. As the baseline SR substantially decreases with an increase in elevation angle, it is implied that the highest SR "recovery" is achieved for the highest elevation angle, as the baseline SR is increased by about 50%.

VI.   Conclusions

The effectiveness of hybrid flow control and its passive and active components on the flow over a turret is investigated experimentally at $M = 0.3$–0.5 and $Re_D = 4.4$–7.4×10^6. The main motivation for this work is the objective of suppressing optical aberrations within the separated flow over a conformal optical window embedded in the hemispherical cap of a cylindrical turret model. Active flow control is effected via direct, small-scale actuation by arrays of synthetic jets distributed upstream from the optical window. In a case of hybrid flow control, a forward passive partition plate is added for a global flow alteration in tandem with active control. Single-partition-plate geometry is tested in two lengths: partitions that extend $R/2$ and R upstream from the turret, which are mounted at the interface between the cylinder and hemisphere. The effects of
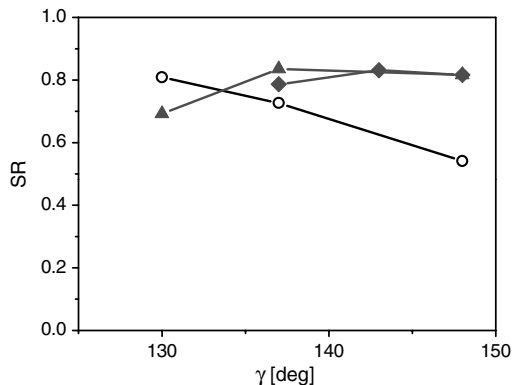

Fig. 22   Strehl ratio with the turret elevation angle for the baseline (circle) and the hybrid flow control using the short (triangle) and long partition plate (diamond).

actuation on the base flow at three elevation angles of the optical window are assessed from the surface static pressure distributions, oil-flow visualization, and hot-film measurements within the separated flow.

It is shown that spatial redistribution of the control actuator modules relative to the previous studies enhances their effectiveness in a static sense (separation delay), although the main effect of the active control remains in the dynamic suppression of turbulent oscillations in the shear layer, once the flow separates. The effects of redistribution of the actuator modules in an arc form upstream from the optical window, rather than wrapped around it, are consistent with the previous studies on the flow control by arced arrays of synthetic jet actuators on turrets. Namely, any outward extension of the arc does not only effect the flow at its termination side, but also incrementally enhances any previous favorable effect inward, toward the symmetry plane.

Surface oil-flow visualization of the baseline flows over the modified turret geometry by additions of either passive partition plate showed significant reduction in the wake reattachment length for about 30% at $M = 0.3$. Induced necklace vortices at the upstream juncture between the plates and hemisphere are shown to displace the stagnation point on the hemisphere from $\gamma = 0$ to 9 and $17°$ for the long and short partition plates, respectively. Static pressure measurements indicate further that both partition plates induce significant separation delay $\Delta\gamma_s \approx 20°$ across the optical window. Moreover, such a strong separation delay is persistent over the full span of the tested Mach numbers $M = 0.3$–0.5. Spanwise static pressure distributions upstream from the optical window indicate that passive flow control induces stronger separation delay than active flow control, while their simultaneous application in the hybrid control mode yields the best results. Furthermore, it is interesting to note that hybrid control recovers almost identical static pressure fields upstream from the optical window, regardless of which partition plate is used. Spectral characterization of the separated flow by measurements of the velocity fluctuations showed that addition of the partition plate to the base turret geometry induces a near-field effect that varies across the shear layer, but that eventually suppresses broadband fluctuation energy across the shear layer further downstream from the turret. Such a favorable effect is further enhanced by addition of active flow control in the hybrid control configuration, for which it is measured that it always further reduces broadband energy of the velocity fluctuations, regardless of the downstream and cross-stream position within the shear layer. Overall, it is concluded that hybrid flow control always induces the best aerodynamic alteration of the wake in any of the aspects that the active, passive, and hybrid flow control were analyzed. Furthermore, only subtle differences are measured between the two partition plates that were tested, with both of these passive modifications resulting in substantial and similar flow-separation delay and suppression of the turbulent energy within the ensuing wake.

Although accompanying in-depth aero-optical flow characterizations are the subject of a separate paper, some overall results are shown here, verifying that measured aerodynamic improvements due to the hybrid control are related to the enhancement in the aero-optical transmission through the controlled flow. Thus, it is shown that the Strehl ratio of the beam traversing the separated flow under the hybrid control becomes nearly independent of the elevation angle between $\gamma = 137$–$148°$. Knowing that the baseline Strehl ratio significantly decreases with an increase in elevation angle, it follows that the highest improvement in the Strehl ratio of about 50% is achieved for the highest tested elevation angle.

Acknowledgments

References

[1] Sutton, G., "Aero-Optical Foundations and Applications," *AIAA Journal*, Vol. 23, 1985, pp. 1525–1537.
doi:10.2514/3.9120

[2] J. Gilbert, and L. J. Otten, (eds), *Aero-Optical Phenomena*, Progress in Astronautics and Aeronautics, Vol. 80, AIAA, New York, 1982.

[3] Tatarskii, V. I., and Zavorotnyi, V. U., "Wave Propagation in Random Media with Fluctuating Turbulent Parameters," *Journal of the Optical Society of America A (Optics, Image Science and Vision)*, Vol. 2, No. 12, 1985, pp. 2069–2076.
doi:10.1364/JOSAA.2.002069

[4] Jumper, E. J., and Fitzgerald, E. J., "Recent advances in aero-optics," *Progress in Aerospace Sciences*, Vol. 37, 2001, pp. 299–339.
doi:10.1016/S0376-0421(01)00008-2

[5] Dimotakis, P. E., Catrakis, H. J., and Fourguette, D. C., "Flow Structure and Optical Beam Propagation in High-Reynolds-Number Gas-Phase Shear Layers and Jets," *Journal of Fluid Mechanics*, Vol. 433, 2001, pp. 105–134.

[6] Fitzgerald, E. J., and Jumper, E. J., "The Optical Distortion Mechanism in a Nearly Incompressible Free Shear Layer," *Journal of Fluid Mechanics*, Vol. 512, 2004, pp. 153–189.

[7] Hunt, J. C. R., Abell, C. J., Peterka, J. A., and Woo, H., "Kinematical Studies of the Flows Around Free or Surface-Mounted Obstacles; Applying Topology to Flow Visualization," *Journal of Fluid Mechanics*, Vol. 86, 1978, pp. 179–200.
doi:10.1017/S0022112078001068

[8] Leder, A., Grebin, U., Hassel, E., Kashkoul, Y., and Ackl, A., "3-D-Flow Structures Behind a Circular Cylinder with Hemispherical Head Geometry," *Proceedings in Applied Mathematics and Mechanics*, Vol. 3, 2003, pp. 40–43.
doi:10.1002/pamm.200310311

[9] Vukasinovic, B., Brzozowski, D., and Glezer, A., "Fluidic Control of Separation over a Hemispherical Turret," *AIAA Journal*, Vol. 47, No. 9, 2009, pp. 2212–2222.
doi:10.2514/1.41920

[10] Woszidlo, R., Taubert, L., and Wygnanski, I., "Manipulating the Flow over Spherical Protuberances in a Turbulent Boundary Layer," *AIAA Journal*, Vol. 47, No. 2, 2009, pp. 437–450.
doi:10.2514/1.39930

[11] Snyder, C. H., Franke, M. E., and Masquelier, M. L., "Wind-Tunnel Tests of an Aircraft Turret Model," *Journal of Aircraft*, Vol. 37, 2000, pp. 368–376.
doi:10.2514/2.2625

[12] Gordeyev, S., Jumper, E. J., Ng, T. T., and Cain, A. B., "The Optical Environment of a Cylindrical Turret with a Flat Window and the Impact of Passive Control Devices," AIAA Paper 2005-4657, 2005.

[13] Purhoit, S. C., Shang, J. S., and Hankey, W. L., "Effect of Suction on the Wake Structure of a Three-Dimensional Turret," AIAA Paper 83-1738, 1983.

[14] Vukasinovic, B., and Glezer, A., "Control of a Separating Flow over a Turret," AIAA Paper 2007-4506, 2007.

[15] Vukasinovic, B., Glezer, A., Gordeyev, S., Jumper, E., and Kibens, V., "Active Control and Optical Diagnostics of the Flow over a Hemispherical Turret," AIAA Paper 2009-598, 2008.

[16] Morgan, P., and Visbal, M., "Numerical Simulations Investigating Control of Flow over a Turret," AIAA Paper 2009-574, 2009.

[17] Vukasinovic, B., Glezer, A., Gordeyev, S., Jumper, E., and Kibens, V., "Fluidic Control of a Turret Wake, Part I: Aerodynamic Effects," AIAA Paper 2009-816, 2009.

[18] Gordeyev, S., Jumper, E., Vukasinovic, B., Glezer, A., and Kibens, V., "Fluidic Control of a Turret Wake, Part II: Aero-Optical Effects," AIAA Paper 2009-817, 2009.

[19] Wallace, R., Andino, M., Glauser, M., Camphouse, C., Schmit, R., and Myatt, J., "Flow Characteristics of Active Control Around a 3-D Turret," AIAA Paper 2009-573, 2009.

[20] Gordeyev, S., and Jumper, E., "Fluid Dynamics and Aero-Optical Environment Around Turrets," AIAA Paper 2009-4224, 2009.

[21] Vukasinovic, B., Glezer, A., and Rusak, Z., "Dissipative Small-Scale Actuation of a Turbulent Shear Layer," *Journal of Fluid Mechanics*, Vol. 656, 2010, pp. 51–81.
doi:10.1017/S0022112010001023

[22] Zubair, F. R., Freeman, A. P., Piatrovich, S., Shockro, J., Ibrahim, Y. N., and Catrakis, H. J., "Large Scale Turbulence Suppression Control for Direct Reduction of Aero-Optical Aberrations," AIAA Paper 2007-4008, 2007.

[23] Oljaca, M., and Glezer, A., "The Effects of Induced Dissipative Small-Scale Motions and Mixing on Optical Distortion in a Plane Shear Layer," *Journal of Fluid Mechanics*, Vol. 619, 2009, pp. 295–329.

doi:10.1017/S0022112008004497

[24] Schonberger, J. R., Fuhs, A. E., and Mandigo, A. M., "Flow Control for an Airborne Laser Turret," *Journal of Aircraft*, Vol. 19, No. 7, 1982, pp. 531–537.
doi:10.2514/3.57426

[25] Gordeyev, S., Jumper, E., Vukasinovic, B., Glezer, A., and Kibens, V., "Hybrid Control of a Turret Wake, Part II: Aero-Optical Effects," AIAA Paper 2010-438, 2010.

[26] Achenbach, E., "Experiments on the Flow Past Spheres at Very High Reynolds Numbers," *Journal of Fluid Mechanics*, Vol. 54, No. 3, 1972, pp. 565–575.
doi:10.1017/S0022112072000874

A. Naguib
Associate Editor